Research Square

Preprints are preliminary reports that have not undergone peer review.
They should not be considered conclusive, used to inform clinical practice,
or referenced by the media as validated information.

Predictive tactile coding in a memristive neuromorphic tactile system

Xuemeng Li
Beihang University
Zheng Miao
Peking University
Shuo Gao
Beihang University
Chenyu Tang
Peking University
Lingyi Kong
Beihang University
Wentian Yi
University of Cambridge
Edoardo Occhipinti
University College London
Yubiao Luo
Peking University
Yongxiang Li
Peking University
Xiaoyu Guo
City University of Hong Kong
Zhong Sun
Peking University
Luigi Giuseppe Occhipinti
L.G.Occhipinti@lboro.ac.uk
Loughborough University

Article

Keywords:

Posted Date: May 26th, 2026

DOI: https://doi.org/10.21203/rs.3.rs-9562092/v1

License: This work is licensed under a Creative Commons Attribution 4.0 International License.
Read Full License

Additional Declarations: No competing interests reported.

Predictive tactile coding in a memristive neuromorphic tactile system

Authors

Xuemeng Li[1], Zheng Miao[2,3], Shuo Gao[1], Chenyu Tang[4,5], Lingyi Kong[1], Wentian Yi[5], Edoardo Occhipinti[6], Yubiao Luo[2,3], Yongxiang Li[2,3], Xiaoyu Guo[7], Zhong Sun[2,3], Luigi Giuseppe Occhipinti[5,8]

Affiliations

1 School of Instrumentation and Optoelectronic Engineering, Beihang University, 100191, Beijing, China

2 Institute for Artificial Intelligence, Peking University, Beijing 100871, China

3 School of Integrated Circuits, Peking University, Beijing 100871, China

4 School of Electronic and Computer Engineering, Peking University, Shenzhen 518055, China

5 Department of Engineering, University of Cambridge, Cambridge CB3 0FA, UK

6 Department of Mechanical Engineering, University College London, London WC1E 6BT, UK

7 Department of Mechanical Engineering, City University of Hong Kong, 83 Tat Chee Avenue, Hong Kong

8 School of Mechanical, Electrical and Manufacturing Engineering, Loughborough University, Loughborough LE11 3TU, UK

Corresponding to: Shuo Gao (shuo_gao@buaa.edu.cn), Xiaoyu Guo (xiaoyguo@cityu.edu.hk), Zhong Sun (zhong.sun@pku.edu.cn) and Luigi Giuseppe Occhipinti (l.g.occhipinti@lboro.ac.uk).

These authors contributed equally: Xuemeng Li, Zheng Miao, Shuo Gao.

Abstract

Flexible tactile electronics have progressed rapidly in wearable electronics, electronic skin, tactile sensing materials and neuromorphic sensory devices, yet most artificial touch systems still interpret contact only after the signal has already been measured. Such a reactive mode supports static recognition, but it is less suited to continuous interaction, where tactile sensing is embedded in the evolving contact process and must follow how surface morphology changes during scanning. Inspired by predictive processing in biological sensory systems, in which incoming signals are interpreted against an internally generated expectation of the next sensory state, we introduce a predictive tactile neuromorphic system that couples a 44×44 flexible tactile array to an 8×8 memristive array for one-step next-state estimation and mismatch-based tactile inference. We program the learned latent-state transition matrix into the memristive conductance matrix so that the current encoded tactile state can be projected in hardware to its predicted successor. In experiments, a flexible pressure sensor mounted on a robotic fingertip records the evolving contact fields during sliding. Each tactile frame is compressed into an 8-dimensional latent representation and propagated through a programmed memristive conductance matrix to generate the predicted next tactile state, which is then compared with the measured next state to produce a normalized mismatch score that quantifies the deviation between expected and observed tactile evolution. Across 1,800 scan sequences spanning smooth, coarse periodic, and fine periodic surface states with matched local violations, the system maintains low mismatch during regular tactile evolution and generates pronounced mismatch peaks when local continuity is broken. The pooled anomaly-discrimination performance reaches an ROC AUC of 0.992. The proposed predictive framework achieves a normal-region prediction error of 0.018 a.u., where normal-region refers to scan segments outside the disturbed zone, and maintains AUCs of 0.96, 0.91, and 0.87 under three speed/force perturbation settings, compared with 0.78, 0.70, and 0.66 for the no-temporal-context baseline. These results show that expectation-driven tactile inference can be embedded directly into the sensing-computing pathway and can support compact neuromorphic touch systems for robotic inspection, dexterous manipulation, and adaptive human-machine interfaces operating under continuously changing contact conditions.

I Introduction

Flexible tactile electronics are becoming an increasingly important interface for intelligent robots, neuroprosthetic devices, wearable systems, machine skins, and touch-based human-machine interfaces [1-4]. Over the past decade, major advances in tactile sensing materials, epidermal electronics, high-density pressure arrays, multifunctional smart skins, and intelligent soft robotic skins have expanded the scope of artificial touch from simple contact transduction to distributed spatiotemporal perception [5-11]. These developments have improved tactile resolution, mechanical compliance, and signal accessibility. Even so, many artificial tactile systems still operate in a largely measurement-driven way: contact is acquired, a feature vector is extracted, and interpretation follows through classification, regression, or thresholding [12-17]. This workflow is effective in many settings. During continuous interaction, however, the significance of a tactile event often depends on whether the incoming signal matches the tactile evolution that the system should already expect, which makes subtle but meaningful local disruptions difficult to distinguish from ongoing background contact dynamics.

Predictive coding and internal forward models provide a natural framework for this problem [18-21]. In this framework, higher-order circuits generate expectations about upcoming sensory states, and the difference between predicted and measured input carries information that can be used for inference and control [21-23]. This principle has often been discussed in visual and motor systems [18-23], and growing evidence suggests that it is also central to touch [24-27]. Self-generated tactile signals are attenuated when their sensory consequences are predictable [24,25]. Layer-resolved studies in human somatosensory cortex have further supported the coexistence of sensory input and predictive feedback in tactile processing [26], and omission-based paradigms have shown that somatosensory systems encode expected events even when the expected tactile input is absent [27]. Haptic and whisker-based studies likewise indicate that touch emerges through sequential sensorimotor interaction, with perception shaped by how local signals unfold over time during active contact [28,29]. Together, these observations suggest that tactile processing depends not only on afferent input, but also on an internally maintained expectation of what should be felt next.

These physiological insights are particularly relevant for artificial touch during sliding and probing. A local violation on a surface may be small in absolute amplitude and still remain highly informative because it interrupts a previously regular tactile trajectory. On a smooth surface, the expected tactile field may evolve gently and continuously. On a periodic textured surface, the expected tactile field may already contain structured oscillatory components. In both cases, the essential question is whether the measured signal is consistent with the expected tactile state implied by the current one. A predictive tactile architecture therefore offers a way to convert continuous touch into a comparison between expected and observed tactile evolution, so that subtle local departures can become more detectable even when the underlying surface state changes.

To realize this expectation-comparison loop in compact hardware, we need a physical substrate that can transform the current tactile state into a near-future estimate with low overhead and good repeatability. Memristive devices are well suited to this requirement [30-32]. Since the memristor was first proposed as a fundamental circuit element [30] and later physically realized in nanoscale resistive devices [31], memristive systems have become important candidates for synaptic electronics, analog state storage, in-memory computation, and human-like neural computing [33-35]. Their conductance-based operation makes them especially suitable for projection and temporal transformation, where a current encoded state can be mapped directly to an expected next state through a programmed physical matrix [36-39]. This feature is particularly relevant for tactile prediction because the core computation is inherently temporal: the present tactile state has to be transformed into a near-future tactile expectation in a compact and repeatable manner.

Recent studies have also begun to connect memristive and neuromorphic hardware with intelligent perception. Memristive elements have been used to emulate nociceptive responses [40], self-healable neuromorphic sensory signal processing [41], adaptive perception in unstructured environments [42], and crossmodal in-sensor computing [43]. At the system level, resistive memory devices support in-memory vector-matrix operations that reduce data movement and bring computation closer to the sensor [44,47]. Related organic and ionic devices have demonstrated low-voltage neuromorphic behavior with direct sensory relevance [45], while more recent neuromorphic sensory hardware has shown that predictive and ultrafast perception can be physically embedded in non-von-Neumann substrates [46].

Here we present a predictive tactile neuromorphic system organized around a flexible tactile array, a shared tactile encoder, and an 8×8 memristive array. A flexible pressure sensor mounted on a

robotic fingertip records evolving tactile fields during sliding interaction. Each tactile frame is encoded into an 8-dimensional latent state comprising total contact intensity, peak response, effective contact area, pressure-centroid coordinates, spatial dispersion, left-right asymmetry, and short-window temporal variation. We pass the current latent state through a programmed 8×8 memristive conductance matrix to generate the predicted next latent state, while we encode the measured next tactile frame in parallel into the same latent space. We then compare the predicted and measured next states through a normalized mismatch score, which quantifies the deviation between the predicted next tactile state and the measured next tactile state, and we identify unexpected tactile events using a decision threshold τ selected on the validation set. The study is designed around three nominal surface states—smooth, coarse periodic, and fine periodic—and matched local-violation conditions embedded within each state. This formulation shifts the task from single-condition anomaly screening to state-dependent predictive tactile inference. The tactile front end is built on a flexible thin-film piezoresistive tactile array that enables conformal and spatially resolved contact readout during sliding interaction. The tactile front end provides stable spatiotemporal sensing across 0 – 40 kPa, bending radii down to 10 mm, and 10^5 loading cycles. The predictive hardware is realized with an 8×8 one-transistor-one-resistor (1T1R) metal-oxide memristive array using a Pt/HfO_2/Ta/Pt device stack. The memristive predictor shows accurate programmed projection with (r = 0.972), fast 30 ns switching, and stable multilevel conductance modulation. Across the state-dependent benchmark, we obtain a pooled anomaly Receiver Operating Characteristic Area Under the Curve (ROC AUC) of 0.992, reduce the normal-region prediction error to 0.018 a.u., where normal-region denotes scan segments outside the disturbed zone, and achieve a mean distance-to-detection of 0.32 mm, defined here as the scan distance between the physical onset of a local violation and its first algorithmic detection.

II. Results

System architecture for predictive tactile inference

We integrated a flexible tactile array, a latent-state encoder, and an 8×8 memristive predictor into a single inference pipeline (Fig. 1). During sliding contact, the tactile patch mounted on the underside of the robotic fingertip records the evolving pressure field at the contact interface. Each tactile frame X_t is transformed into an 8-dimensional latent vector z_t, which is then projected by the memristive array to generate the predicted next state $\hat{z}_{t+1}$. We encode the measured next frame X_{t+1} in parallel as z_{t+1}, and we convert the discrepancy between $\hat{z}_{t+1}$ and z_{t+1} into a normalized mismatch score for event detection.

In this configuration, we perform prediction on the latent tactile trajectory instead of the raw pressure map. The hardware predictor therefore operates on local temporal continuity: under regular contact, successive encoded states remain close to the learned transition, whereas a local disturbance produces a rapid increase in mismatch. This arrangement differs from frame-wise thresholding or static template comparison, where the decision is made directly from the measured signal at a single instant. Here we interpret the measured state against the state that should follow from the preceding one.

The revised benchmark places this predictive step at the center of the task. Instead of testing only smooth-background anomaly screening, we evaluated the system across smooth, coarse-periodic, and fine-periodic surface states, each with a matched local-violation condition. The role of the

predictor is therefore to preserve the correct next-state evolution for multiple nominal tactile regimes and to produce a strong residual only when that evolution is locally interrupted.

Tactile front end and memristive predictor support stable next-state estimation

Stable next-state inference first requires a front end that can resolve the spatial structure of evolving contact fields. The flexible tactile sensor used here is a 44×44 pressure array with 1,936 sensing elements distributed over a 26 mm×26 mm active area (Fig. 2a,b). Under sliding contact, the array captures compact smooth-contact hotspots, lobe splitting during crack crossing, localized redistribution near protrusions, and stripe-like modulation on periodic surfaces (Fig. 2c). These patterns remain spatially distinguishable across the contact states used in this study and provide the basis for latent-state encoding and next-state comparison.

The front end remains stable over the operating range used in the experiments. Pressure calibration over 0 – 40 kPa shows a monotonic response, with a loading-unloading hysteresis of 5.4% (Fig. 2d). Bending tests performed at radii of 30, 20, and 10 mm give a maximum deviation below 5.1% from the flat-state response (Fig. 2e). Under cyclic loading at 15 kPa and 2 Hz, the normalized output drift after 10^5 cycles is 4.2% (Fig. 2f). These results indicate that the sensor provides reproducible spatiotemporal readout during repeated low-force scanning.

We implement the predictive projection with an 8×8 memristive array (Fig. 3). When we apply the encoded tactile state to the programmed conductance matrix, the hardware output reproduces the target projection with a Pearson correlation coefficient of 0.972 and an RMSE of 0.043 (Fig. 3a). The array exhibits repeatable bipolar switching, multilevel conductance programming over approximately 50 – 330 μS, and fast SET/RESET operation under 30 ns pulses (Fig. 3c – g). These characteristics are sufficient to support the one-step latent-state mapping used throughout the experiments.

Together, the tactile front end and the memristive predictor provide the two experimental conditions required for the remainder of the study: stable tactile sequences at the sensor level and hardware-realized next-state projection at the predictor level. On that basis, we shift the task from direct signal inspection to mismatch-based detection of local departures from ongoing tactile evolution.

Local violations emerge as structured residuals across different surface states

We next examined how the predictor behaves under three nominal surface states (smooth, coarse-periodic, and fine-periodic) each with a matched local-violation condition (Fig. 4). For the smooth regular surface, the predicted next tactile map remains close to the measured next map, and the residual stays weak over the contact region. When we introduce a local crack-like defect into the same smooth background, the measured map develops a confined distortion along the defect while the predicted map preserves the smooth-contact progression, giving rise to a compact residual centered at the disturbed region.

A similar pattern appears on the coarse-periodic surface. In the regular condition, the predicted and measured next states both retain the multi-lobed structure imposed by the periodic background, and only a weak residual remains. Once a local violation is embedded in the same surface, the measured state departs locally from that lobe pattern and the residual becomes sharply localized. The fine-periodic condition shows the same behavior at a smaller spatial scale. The regular scan preserves the dense stripe-like modulation in both prediction and measurement, whereas the

violated scan introduces a local deformation that appears as a concentrated residual superimposed on the periodic background.

Across all three regimes, the residual does not become strong simply because the background itself is more structured. Smooth, coarse-periodic, and fine-periodic scans each retain their own next-state pattern under regular contact. The residual becomes prominent when the measured sequence deviates locally from the evolution associated with that surface state. This behavior is consistent throughout the representative examples in Fig. 4, where the mismatch remains confined to the disturbed region instead of spreading broadly across the full contact field.

Predictive mismatch yields clear separation from regular scans

The trajectory-level results are summarized in Fig. 5a. For all three surface states, the regular scans maintain a low mismatch baseline along the scan path, whereas the violated scans produce narrow peaks centered near the disturbed region. The smooth condition gives the lowest baseline. The coarse-periodic and fine-periodic conditions show slightly broader low-level fluctuations, reflecting the richer frame-to-frame dynamics of regular textured contact, while the mismatch peak associated with the local violation remains clearly separated from the corresponding regular trajectory in each case.

The same separation appears in the pooled score distributions (Fig. 5b). Smooth regular scans cluster at the lowest mismatch values. Periodic regular scans occupy a somewhat broader low-mismatch range and still remain distinct from the violated scans collected on the same background type. Introducing a local violation shifts the distributions toward higher scores in both smooth and periodic settings. The ROC inset gives an AUC of 0.992 for the predictive method, compared with 0.907 for the no-temporal-context baseline and 0.812 for the threshold-based baseline.

The quantitative comparison across ablation settings is shown in Fig. 5c. In normal regions, which here denote scan segments outside the disturbed zone, the proposed method yields an average prediction error of approximately 0.018 a.u., lower than the values obtained with no temporal context (~0.032 a.u.), shuffled temporal order (~0.040 a.u.), a static-template baseline (~0.049 a.u.), or amplitude thresholding (~0.064 a.u.). On the anomaly-detection task, the corresponding AUC values are ~0.985, ~0.934, ~0.903, ~0.862, and ~0.816. The proposed method also gives the shortest mean distance-to-detection, that is, the scan distance from the physical onset of the disturbed region to the first threshold crossing, at ~0.32 mm, compared with ~0.60, ~0.75, ~0.85, and ~0.97 mm for the same baselines. Under low-speed/low-force, high-speed/low-force, and high-speed/high-force conditions, the predictive model maintains AUC values of about 0.96, 0.91, and 0.87, whereas the no-temporal-context baseline drops to about 0.78, 0.70, and 0.66. In these panels, the bars represent mean values across repeated evaluations under the same split protocol, and the error bars indicate the corresponding variability.

III. Discussion

We show that predictive tactile coding can be implemented in a hardware system that combines a flexible tactile interface with a memristive temporal predictor. Within this architecture, tactile events are interpreted through the relation between measured and expected contact evolution. We use the current tactile state to generate the expected next state, and we reveal local disturbances through the mismatch between prediction and measurement. The results show that this formulation remains effective across distinct tactile regimes with different intrinsic temporal structures.

This point is important for the revised benchmark. In the earlier smooth-only setting, discrimination could still be attributed in part to the relative simplicity of the background dynamics. In the present design, the system is required to operate across smooth, coarse-periodic, and fine-periodic surface states, each of which imposes a different local evolution on the tactile stream. The predictor therefore has to preserve low mismatch under several distinct forms of regular contact and increase the response only when that state-specific evolution is locally interrupted. Fig. 4 visualizes this process through state-dependent residual localization, and Fig. 5 quantifies the resulting separation, discrimination, and robustness.

The performance gain of the predictive framework can be attributed to two experimentally supported effects. First, the learned transition suppresses the expected component of regular tactile evolution. This effect is reflected by the low normal-region prediction error in Fig. 5c, where scan segments outside the disturbed zone remain close to the predicted next state even when the background changes from smooth to periodic contact. The system therefore does not treat the intrinsic modulation of a textured surface as an anomalous event as long as this modulation follows the learned state-dependent trajectory. Second, the same comparison makes local disruptions visible at their onset, because a crack-like or structurally violated region changes the measured next state before a large absolute pressure difference necessarily accumulates. This interpretation is supported by the localized residual maps in Fig. 4 and by the shorter distance-to-detection in Fig. 5c. Together, these results indicate that the gain comes from comparing the measured tactile stream with its expected temporal continuation, rather than from amplifying raw pressure amplitude alone.

In this system, the memristive array is used as a physical temporal operator rather than as a passive memory block. The programmed conductance matrix directly maps the current latent tactile state to its predicted successor, thereby implementing the one-step forward projection that defines the predictive component of the inference chain. The measured projection fidelity, stable multilevel conductance tuning, and fast switching behavior indicate that this temporal mapping can be carried out in a compact hardware module coupled to the tactile readout path. This hardware role is central to the proposed architecture because the mismatch score is formed only after the current state has been physically transformed into an expected next state.

The present study also has clear limits. The experimental device demonstrates its effectiveness in one-step prediction under controlled linear sliding, with the latent representation intentionally kept compact for this purpose. More complex contact behaviors, including multidirectional scanning, variable compliance, longer temporal dependencies, and closed-loop exploratory interaction, will require richer state representations and predictive models that capture nonlinear transitions, multi-step temporal context, and action-conditioned contact dynamics. In addition, the present architecture remains a hybrid implementation. Moving toward a fully integrated system will require closer co-integration of sensing, readout, and memristive prediction to reduce interconnect overhead and improve system compactness and efficiency.

Within these limits, the obtained results define a mechanism for embedding next-state prediction into tactile hardware. The central contribution lies in organizing tactile inference around the expected evolution of contact under a given surface state and in using mismatch to expose departures from that evolution. This mechanism becomes increasingly valuable as tactile backgrounds grow richer and less well described by static thresholds or single-state templates. The framework described here may therefore support intelligent robotic inspection, adaptive end-

effectors, prosthetic touch interfaces, and teleoperated human-machine systems that must operate continuously under changing contact conditions [48].

IV. Methods

System architecture and signal flow

Our predictive tactile system consists of a flexible tactile front end, a readout-and-control board, and an 8×8 memristive predictor. During sliding contact, the tactile front end records the evolving pressure field at the fingertip-surface interface. Each tactile frame X_t is converted into an 8-dimensional latent vector z_t by a shared encoder. We then apply the latent state z_t to the memristive predictor to generate the expected next state $\hat{z}_{t+1}$. In parallel, we encode the measured next tactile frame X_{t+1} as z_{t+1}. Event detection is performed on the normalized mismatch between $\hat{z}_{t+1}$ and z_{t+1}.

Flexible tactile front end and acquisition settings

We used a commercial flexible piezoresistive sensor (M5027, Changzhou Rouxi Electronic Technology Co., Ltd., China) as the tactile front end. The sensor contains a 44×44 sensing matrix with 1,936 sensing elements distributed over a 26 mm×26 mm active area. The row and column electrode widths are 0.2 mm, and the nominal pitch is 0.6 mm. We mounted the sensing region on the underside of the robotic fingertip using a thin compliant adhesive layer, while the flexible tail was routed to the readout electronics.

Tactile frames were acquired at 200 Hz under a 3.3 V supply and digitized at 12-bit resolution. Pressure maps shown in the figures have been obtained through interpolation of the acquired data to facilitate visualization. All predictive computations are carried out on the encoded tactile data derived from the recorded array output.

Pressure calibration was performed over 0 – 40 kPa using a controlled loading stage. We used loading and unloading traces to estimate hysteresis. Bending stability was evaluated under flat, 30 mm, 20 mm, and 10 mm radii. Cyclic durability was measured at 15 kPa and 2 Hz over 10^5 loading cycles. The values reported in Fig. 2d – f correspond to these measurements.

Surface-state benchmark and scan protocol

Surface-state benchmark analysis was performed comprising six scan conditions: smooth regular, smooth with a local violation, coarse-periodic regular, coarse-periodic with a local violation, fine-periodic regular, and fine-periodic with a local violation. Regular surface conditions were selected to produce progressively richer next-state tactile dynamics during sliding. The local-violation conditions introduce a confined structural disturbance within the matched background state.

All scans were performed over a 20 mm path under a nominal normal force of 0.30 N and a nominal scan speed of 5 mm s^{-1}. For robustness evaluation, we additionally collected scans under three perturbed settings: 3 mm s^{-1} / 0.20 N, 7 mm s^{-1} / 0.20 N, and 7 mm s^{-1} / 0.40 N, corresponding to the low-speed/low-force, high-speed/low-force, and high-speed/high-force conditions shown in Fig. 5c. The disturbed region was positioned near the middle of the scan path so that pre- and post-event segments are included in the same continuous sequence.

A total set of 1,800 scan sequences was collected, with 300 scans for each condition. We performed

data splitting at the physical-sample level to avoid leakage between training, validation, and testing. Regular scans were also used to learn the predictive mapping, using validation data to determine the operating threshold. All reported performance values are obtained from held-out test samples.

Latent-state encoding

Each tactile frame was encoded to an 8-dimensional latent vector using a shared encoder. The encoded variables comprise total contact intensity, peak response, effective contact area, pressure-centroid x coordinate, pressure-centroid y coordinate, spatial dispersion, left-right asymmetry, and short-window temporal variation. The effective contact area was defined as the number of sensing elements above a fixed fraction of the frame maximum. We computed spatial dispersion from the second central moment of the tactile field, and temporal variation from the frame-to-frame difference relative to the immediately preceding frame.

Feature normalization was performed using statistics estimated from the training set only. We then applied the same normalization parameters to validation and test data.

Memristive next-state projection

The one-step predictor was modelled as

$$\hat{z}_{t+1} = Wz_t + c \tag{1}$$

where $W \in \mathbb{R}^{8\times8}$ is the temporal mapping matrix and c is a bias vector. The mapping parameters were estimated using paired latent states extracted from regular training sequences only, where regular sequences from all three nominal surface states are pooled to train one shared transition matrix. After training, the same matrix was programmed into the 8×8 memristive array and used unchanged for all held-out regular and violated scans. During inference, no surface-state label was provided to the predictor; the only input was the 8-dimensional latent tactile state of the current frame. This design was selected to test whether a single hardware forward operator could capture the local temporal continuity of multiple tactile regimes and generate elevated mismatch when the measured trajectory departs from the expected continuation. Violated sequences were excluded from model fitting and used only for validation and held-out evaluation.

We implemented the hardware predictor with an integrated 8×8 1T1R memristive array. The device stack comprises Pt/HfO_2/Ta/Pt. After training, the learned matrix coefficients are converted into conductance targets within the experimentally accessible operating range, and the offset introduced by this conductance mapping compensated during readout. During inference, the normalized latent state z_t is converted into row-input voltages, while the resulting column currents are converted to voltages by transimpedance amplifiers, digitized, and decoded into the predictive next-state representation $\hat{z}_{t+1}$.

To assess projection fidelity we compared the hardware output with the software target projection. The programmed array reproduced the target mapping with a Pearson correlation coefficient of 0.972 and an RMSE of 0.043. Device-level switching, programming, and multilevel conductance characteristics are measured separately, as summarized in Fig. 3.

Mismatch calculation and event detection

For each scan position, we define the predictive mismatch as

$$m_t = \frac{|\hat{z}t+1-zt+1|_2}{|zt+1|_2+\varepsilon} \tag{2}$$

where $\varepsilon = 10^{-6}$ is introduced to avoid numerical instability at very low signal levels. This normalized mismatch score quantifies the deviation between the predicted next latent state and the measured next latent state, and it serves as the primary score throughout the study.

For event detection, a decision threshold τ was determined using the validation set only. By sweeping candidate thresholds over the range of validation mismatch scores and selecting the operating threshold as the value that maximizes Youden's (J) statistic $sensitivity + specificity - 1$ it was possible to differentiate regular from disturbed validation samples. The obtained threshold value was then fixed and applied unchanged to all held-out test data. A disturbed event is considered detected when the mismatch first exceeds τ. Threshold crossing denotes the first scan position at which the mismatch exceeds the validation-defined decision threshold. Distance-to-detection is defined as the scan distance between the physical onset of the disturbed region and this first threshold crossing. Mean distance-to-detection is computed over successfully detected anomalous scans only.

Baselines and quantitative evaluation

Finally, we compared the proposed predictive framework with four baselines in the quantitative analysis: a no-temporal-context baseline, a shuffled-temporal-order baseline, a static-template baseline, and an amplitude-threshold baseline. The no-temporal-context baseline evaluates instantaneous deviation without next-state prediction. The shuffled-temporal-order model retains the same overall structure but destroys the true succession of frames during training. The static-template baseline compares each frame with a reference state derived from regular scans. The amplitude-threshold baseline uses raw peak-pressure magnitude without explicit temporal modeling.

The mismatch trajectories are plotted in Fig. 5a from representative held-out scans under the three nominal surface states. The distributions in Fig. 5b were obtained from pooled frame-level mismatch scores between the held-out regular and violated scans. The ROC value in the inset of Fig. 5b was obtained from the same pooled held-out samples.

For the bar plots in Fig. 5c, we evaluated average prediction error in normal regions, anomaly-detection AUC, and distance-to-detection for all comparison routes under the same split protocol. For robustness analysis, we additionally measured AUC under the three speed/force conditions shown in Fig. 5c. The plotted values represent the mean across repeated evaluations, and the error bars indicate the corresponding variability under the same protocol.

Acknowledgments

S.G. acknowledges funding from National Key Research and Development Program of China (grant No. 2023YFB3208003) and Beihang University (grants No.KG161250 and ZG16S2103). Z.S. acknowledges funding from National Natural Science Foundation of China (grant No. 62572011). L.G.O. acknowledges funding from EPSRC (grants No. EP/W024284/1, EP/P027628/1, EP/K03099X/1), E.O. was partially funded by the Chan Zuckerberg Initiative DAF (grant 2022-316777), an advised fund of the Silicon Valley Community.

Foundation..

Author Contributions

X.L., S.G. and L.G.O. conceived the idea and designed the research. X.L. developed the predictive tactile framework, performed the experiments, analyzed the data, prepared the figures, and drafted the manuscript. Z.M., Y.L., and Z.S. contributed to the memristive hardware implementation, device characterization, and experimental support. C.T., L.K., W.Y., and E.O. contributed to system discussion, experimental interpretation, and manuscript refinement. X.G. and L.G.O. contributed to the interpretation of the results and the refinement of the study. S.G., X.G., Z.S., and L.G.O. supervised the project. All authors discussed the results, revised the manuscript, and approved the final version of the manuscript.

Competing Interests

The authors declare no competing interests.

References

[1] Dahiya, R. S., Metta, G., Valle, M. & Sandini, G. Tactile sensing: from humans to humanoids. IEEE Trans. Robot. 26, 1 – 20 (2010).

[2] Hammock, M. L., Chortos, A., Tee, B. C.-K., Tok, J. B.-H. & Bao, Z. 25th Anniversary Article: The evolution of electronic skin (e-skin): a brief history, design considerations, and recent progress. Adv. Mater. 25, 5997 – 6037 (2013).

[3] Kim, D.-H. et al. Epidermal electronics. Science 333, 838 – 843 (2011).

[4] Tee, B. C.-K. et al. A skin-inspired organic digital mechanoreceptor. Science 350, 313 – 316 (2015).

[5] Wang, C. et al. User-interactive electronic skin for instantaneous pressure visualization. Nat. Mater. 12, 899 – 904 (2013).

[6] Shih, B. et al. Electronic skins and machine learning for intelligent soft robots. Sci. Robot. 5, eaaz9239 (2020).

[7] Dai, Y. & Gao, S. A flexible multi-functional smart skin for force, touch position, proximity, and humidity sensing for humanoid robots. IEEE Sens. J. 21, 8485 – 8495 (2021).

[8] Gao, S., Dai, Y. & Nathan, A. Tactile and vision perception for intelligent humanoids. Adv. Intell. Syst. 4, 2100074 (2022).

[9] Gao, S., Yan, S., Zhao, H. & Nathan, A. Touch-Based Human-Machine Interaction: Principles and Applications (Springer, 2021).

[10] Xu, M., Zhang, J., Dong, C., Tang, C., Hu, F., Malliaras, G. G. & Occhipinti, L. G. Simultaneous isotropic omnidirectional hypersensitive strain sensing and deep learning-assisted direction recognition in a biomimetic stretchable device. Adv. Mater. 37, 2420322 (2025).

[11] Xu, M. et al. Biomimetic metamaterial-based interface for decoding heterogeneous mechanodermal activity. Sci. Adv. 12, eaee2625 (2026).

[12] Sun, F., Lu, Q., Feng, S. & Zhang, T. Flexible artificial sensory systems based on neuromorphic devices. ACS Nano 15, 3875 – 3899 (2021).

[13] Liu, F., Deswal, S., Christou, A., Sandamirskaya, Y., Kaboli, M. & Dahiya, R. Neuro-inspired electronic skin for robots. Sci. Robot. 7, eabl7344 (2022).
[14] Bai, N. et al. A robotic sensory system with high spatiotemporal resolution for texture recognition. Nat. Commun. 14, 7121 (2023).
[15] Kang, K., Kim, K., Baek, J., Lee, D. J. & Yu, K. J. Biomimic and bioinspired soft neuromorphic tactile sensory system. Appl. Phys. Rev. 11, 021328 (2024).
[16] Chen, S. et al. Artificial organic afferent nerves enable closed-loop tactile feedback for intelligent robot. Nat. Commun. 15, 7056 (2024).
[17] Cho, J.-Y. et al. Tactile near-sensor computing systems incorporating hourglass-shaped microstructured capacitive sensors for bio-realistic energy efficiency. npj Flex. Electron. 9, 34 (2025).
[18] Rao, R. P. N. & Ballard, D. H. Predictive coding in the visual cortex: a functional interpretation of some extra-classical receptive-field effects. Nat. Neurosci. 2, 79–87 (1999).
[19] Friston, K. A theory of cortical responses. Philos. Trans. R. Soc. Lond. B Biol. Sci. 360, 815–836 (2005).
[20] Bastos, A. M. et al. Canonical microcircuits for predictive coding. Neuron 76, 695–711 (2012).
[21] Keller, G. B. & Mrsic-Flogel, T. D. Predictive processing: a canonical cortical computation. Neuron 100, 424–435 (2018).
[22] Wolpert, D. M., Ghahramani, Z. & Jordan, M. I. An internal model for sensorimotor integration. Science 269, 1880–1882 (1995).
[23] Wolpert, D. M. & Flanagan, J. R. Motor prediction. Curr. Biol. 11, R729–R732 (2001).
[24] Blakemore, S.-J., Wolpert, D. & Frith, C. Central cancellation of self-produced tickle sensation. Nat. Neurosci. 1, 635–640 (1998).
[25] Bays, P. M., Flanagan, J. R. & Wolpert, D. M. Attenuation of self-generated tactile sensations is predictive, not postdictive. PLoS Biol. 4, e28 (2006).
[26] Yu, Y. et al. Layer-specific activation of sensory input and predictive feedback in the human primary somatosensory cortex. Sci. Adv. 5, eaav9053 (2019).
[27] Dercksen, T. T., Widmann, A., Noesselt, T. & Wetzel, N. Somatosensory omissions reveal action-related predictive processing. Hum. Brain Mapp. 45, e26550 (2024).
[28] Lederman, S. J. & Klatzky, R. L. Hand movements: a window into haptic object recognition. Cogn. Psychol. 19, 342–368 (1987).
[29] Diamond, M. E., von Heimendahl, M., Knutsen, P. M., Kleinfeld, D. & Ahissar, E. 'Where' and 'what' in the whisker sensorimotor system. Nat. Rev. Neurosci. 9, 601–612 (2008).
[30] Chua, L. O. Memristor—the missing circuit element. IEEE Trans. Circuit Theory 18, 507–519 (1971).

[31] Strukov, D. B., Snider, G. S., Stewart, D. R. & Williams, R. S. The missing memristor found. Nature 453, 80 – 83 (2008).

[32] Jo, S. H. et al. Nanoscale memristor device as synapse in neuromorphic systems. Nano Lett. 10, 1297 – 1301 (2010).

[33] Prezioso, M. et al. Training and operation of an integrated neuromorphic network based on metal-oxide memristors. Nature 521, 61 – 64 (2015).

[34] Li, C. et al. Analogue signal and image processing with large memristor crossbars. Nat. Electron. 1, 52 – 59 (2018).

[35] Yang, J. J., Strukov, D. B. & Stewart, D. R. Memristive devices for computing. Nat. Nanotechnol. 8, 13 – 24 (2013).

[36] Xia, Q. & Yang, J. J. Memristive crossbar arrays for brain-inspired computing. Nat. Mater. 18, 309 – 323 (2019).

[37] Sebastian, A., Le Gallo, M., Khaddam-Aljameh, R. & Eleftheriou, E. Memory devices and applications for in-memory computing. Nat. Nanotechnol. 15, 529 – 544 (2020).

[38] Kumar, S., Wang, X., Strachan, J. P., Yang, Y. & Lu, W. D. Dynamical memristors for higher-complexity neuromorphic computing. Nat. Rev. Mater. 7, 575 – 591 (2022).

[39] Wang, S. et al. Memristor-based intelligent human-like neural computing. Adv. Electron. Mater. 9, 2200877 (2023).

[40] Yoon, J. H. et al. An artificial nociceptor based on a diffusive memristor. Nat. Commun. 9, 417 (2018).

[41] John, R. A. et al. Self-healable neuromorphic memtransistor elements for decentralized sensory signal processing in robotics. Nat. Commun. 11, 4030 (2020).

[42] Wang, S. et al. Memristor-based adaptive neuromorphic perception in unstructured environments. Nat. Commun. 15, 4671 (2024).

[43] Li, Z. et al. Crossmodal sensory neurons based on high-performance flexible memristors for human-machine in-sensor computing system. Nat. Commun. 15, 7275 (2024).

[44] Ielmini, D. & Wong, H.-S. P. In-memory computing with resistive switching devices. Nat. Electron. 1, 333 – 343 (2018).

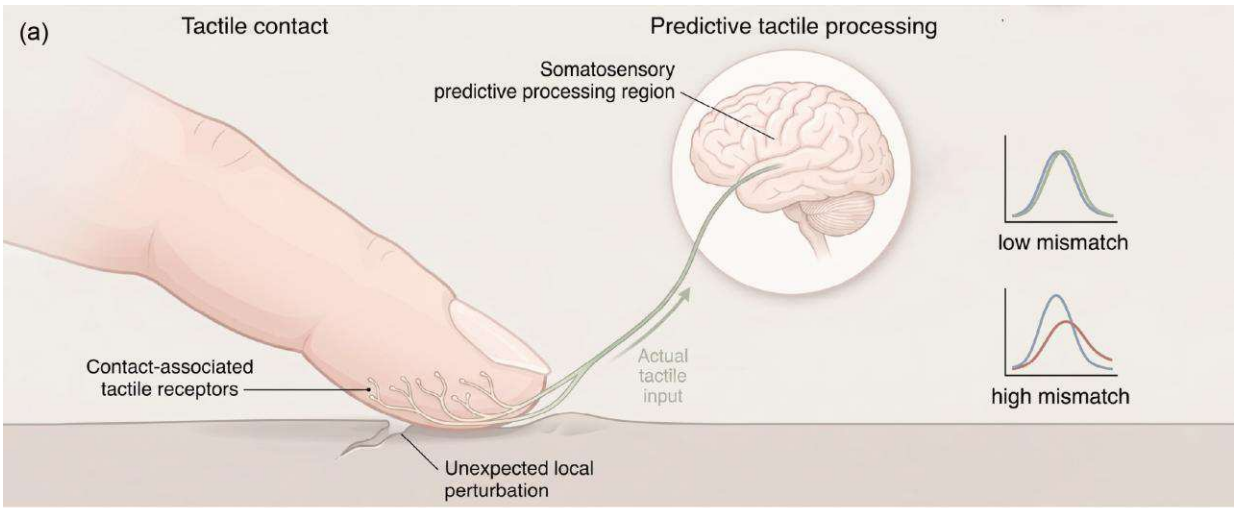
[45] van de Burgt, Y. et al. A non-volatile organic electrochemical device as a low-voltage artificial synapse for neuromorphic computing. Nat. Mater. 16, 414 – 418 (2017).

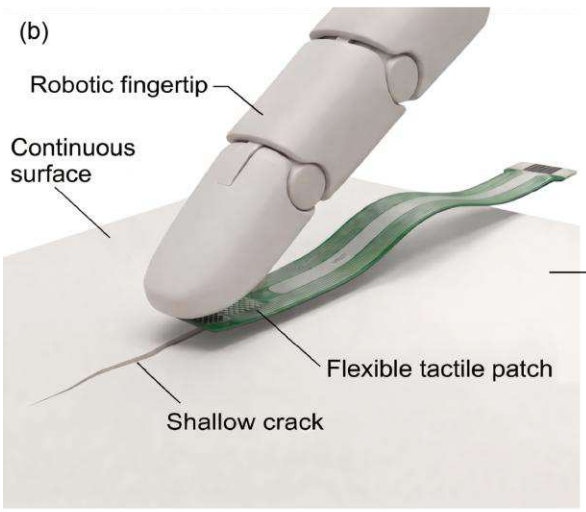
[46] Wang, S. et al. Ultrafast visual perception beyond human capabilities enabled by motion analysis using synaptic transistors. Nat. Commun. 17, 1215 (2026).

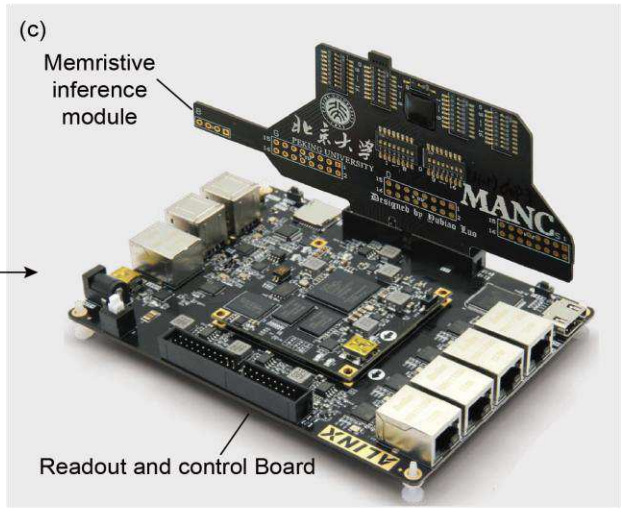
[47] Le Gallo, M. et al. In-memory computing with resistive memory devices. Nat. Electron. 1, 246 – 253 (2018).

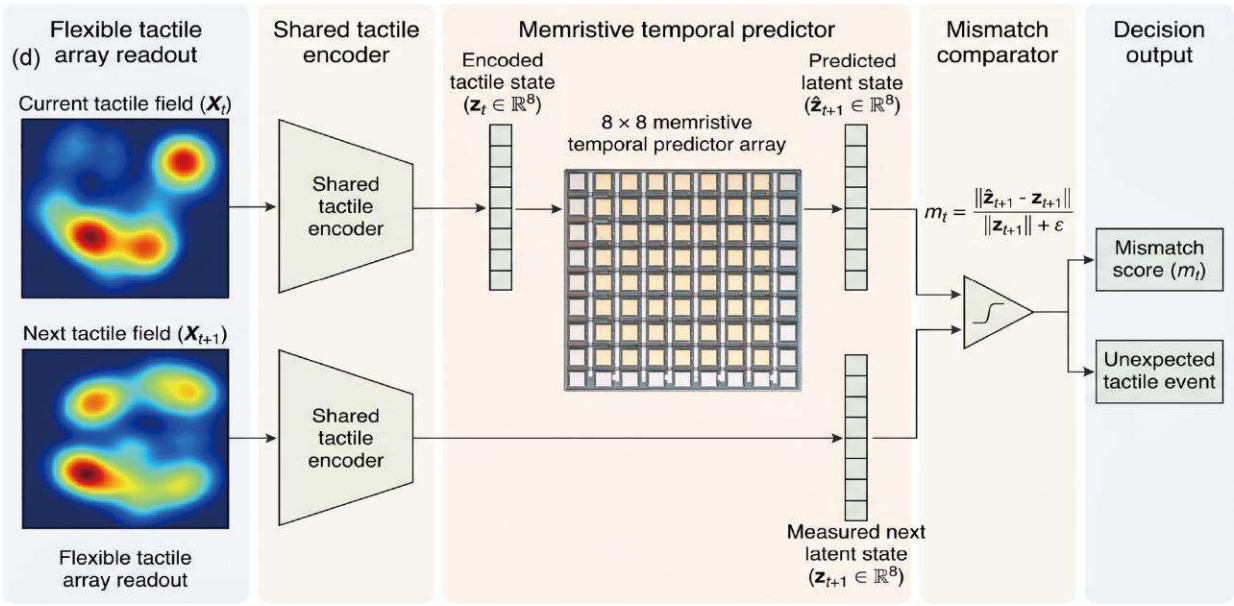
[48] Chu, M. et al. Multisensory fusion, haptic, and visual feedback teleoperation system under IoT framework. IEEE Internet Things J. 9, 19717 – 19727 (2022).

Figures


(a)
Tactile contact
Predictive tactile processing
Somatosensory predictive processing region
low mismatch
high mismatch
Contact-associated tactile receptors
Actual tactile input
Unexpected local perturbation


(b)
Robotic fingertip
Continuous surface
Flexible tactile patch
Shallow crack


(c)
Memristive inference module
Readout and control Board


(d)
Flexible tactile array readout
Current tactile field (X_t)
Next tactile field (X_{t+1})
Flexible tactile array readout
Shared tactile encoder
Shared tactile encoder
Memristive temporal predictor
Encoded tactile state ($z_t \in \mathbb{R}^8$)
8 × 8 memristive temporal predictor array
Predicted latent state ($\hat{z}_{t+1} \in \mathbb{R}^8$)
Measured next latent state ($z_{t+1} \in \mathbb{R}^8$)
Mismatch comparator
$m_t = \frac{\|\hat{z}_{t+1} - z_{t+1}\|}{\|z_{t+1}\| + \varepsilon}$
Decision output
Mismatch score (m_t)
Unexpected tactile event

517

Figure 1 | Predictive tactile system concept and hardware architecture. (a) Biological motivation of predictive tactile processing, in which unexpected local perturbations produce elevated mismatch between expected and actual tactile input. **(b)** Robotic fingertip carrying a flexible tactile patch during contact with a shallow crack. **(c)** Photograph of the memristive inference module and readout/control board. **(d)** Hardware workflow of the predictive tactile system: current tactile field $\boldsymbol{X_t}$ and measured next tactile field $\boldsymbol{X_{t+1}}$ are encoded into an 8-dimensional latent space, the current latent state is projected through an 8×8 memristive temporal predictor to generate $\hat{\boldsymbol{z}}_{\boldsymbol{t+1}}$, and the normalized mismatch between $\hat{\boldsymbol{z}}_{\boldsymbol{t+1}}$ and $\boldsymbol{z_{t+1}}$ is used for unexpected tactile event detection.

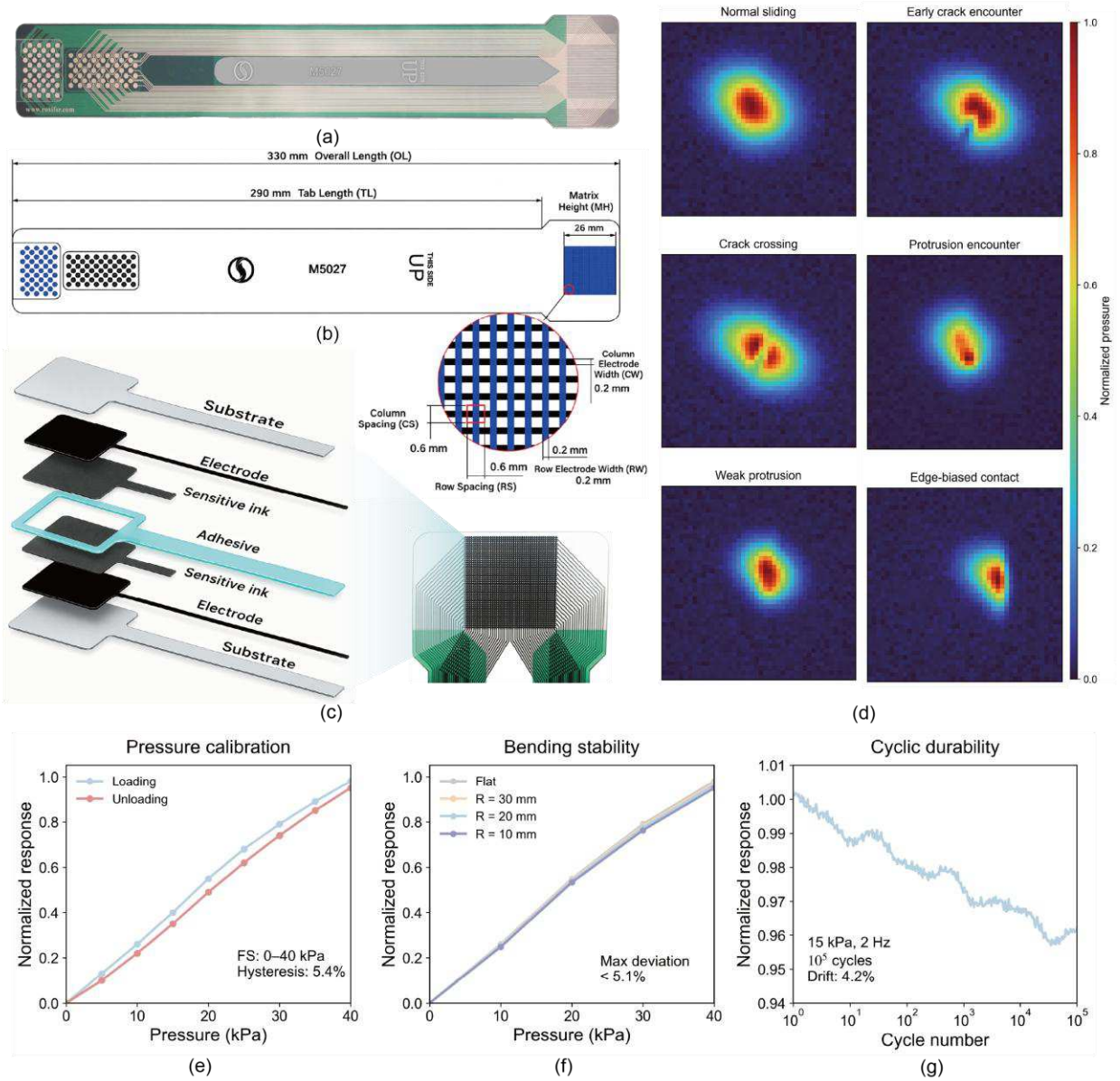


Figure 2 | Flexible tactile front end, representative contact patterns, and sensor stability. (a) Photograph of the M5027 flexible tactile sensor. **(b)** Structural and dimensional details of the tactile array, including multilayer stack and electrode geometry. **(c)** Representative normalized tactile maps acquired from smooth regular contact, smooth contact with a local violation, coarse-periodic regular contact, coarse-periodic contact with a local violation, fine-periodic regular contact, and fine-periodic contact with a local violation. **(d)** Pressure calibration under loading and unloading over 0 – 40 kPa. **(e)** Bending stability under flat, 30 mm, 20 mm, and 10 mm radii. **(f)** Cyclic durability over 10^5 cycles at 15 kPa and 2 Hz.

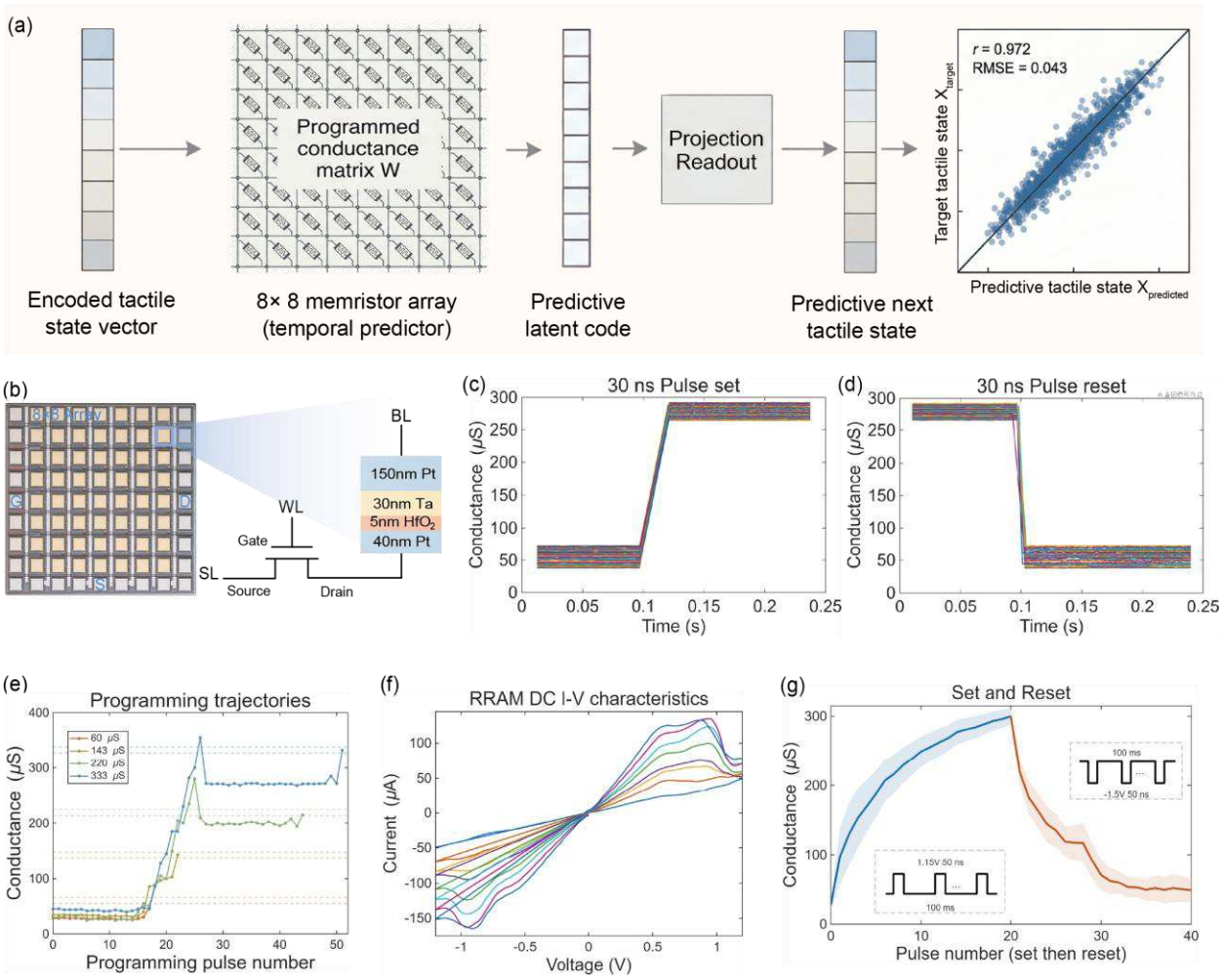


Figure 3 | Memristive temporal predictor and device characteristics. (**a)** Predictive projection through the programmed 8 × 8 memristor array, together with the agreement between hardware output and target predictive tactile state. **(b)** Optical image of the array and device stack schematic. **(c,d)** Fast 30 ns SET and RESET behavior. **(e)** Programming trajectories toward representative multilevel conductance states. **(f)** DC I – V characteristics of the RRAM device. **(g)** Pulse-number-dependent gradual SET and RESET modulation.

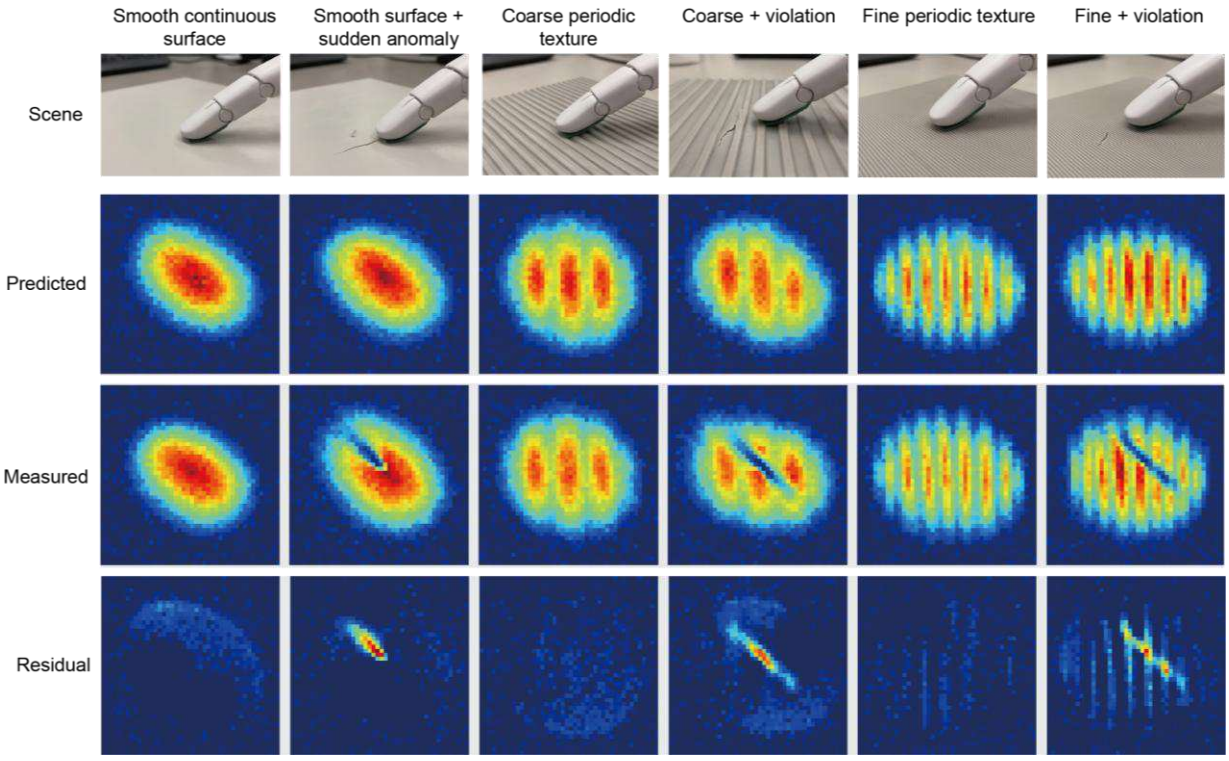


Figure 4 | State-dependent predictive mismatch visualized across regular and violated tactile regimes. Representative scan scenes for smooth regular, smooth with a local violation, coarse-periodic regular, coarse-periodic with a local violation, fine-periodic regular, and fine-periodic with a local violation. For each scene, the predicted next tactile map, measured next tactile map, and residual map are shown to illustrate how local violations emerge as spatially confined mismatch against the corresponding state-specific tactile evolution.

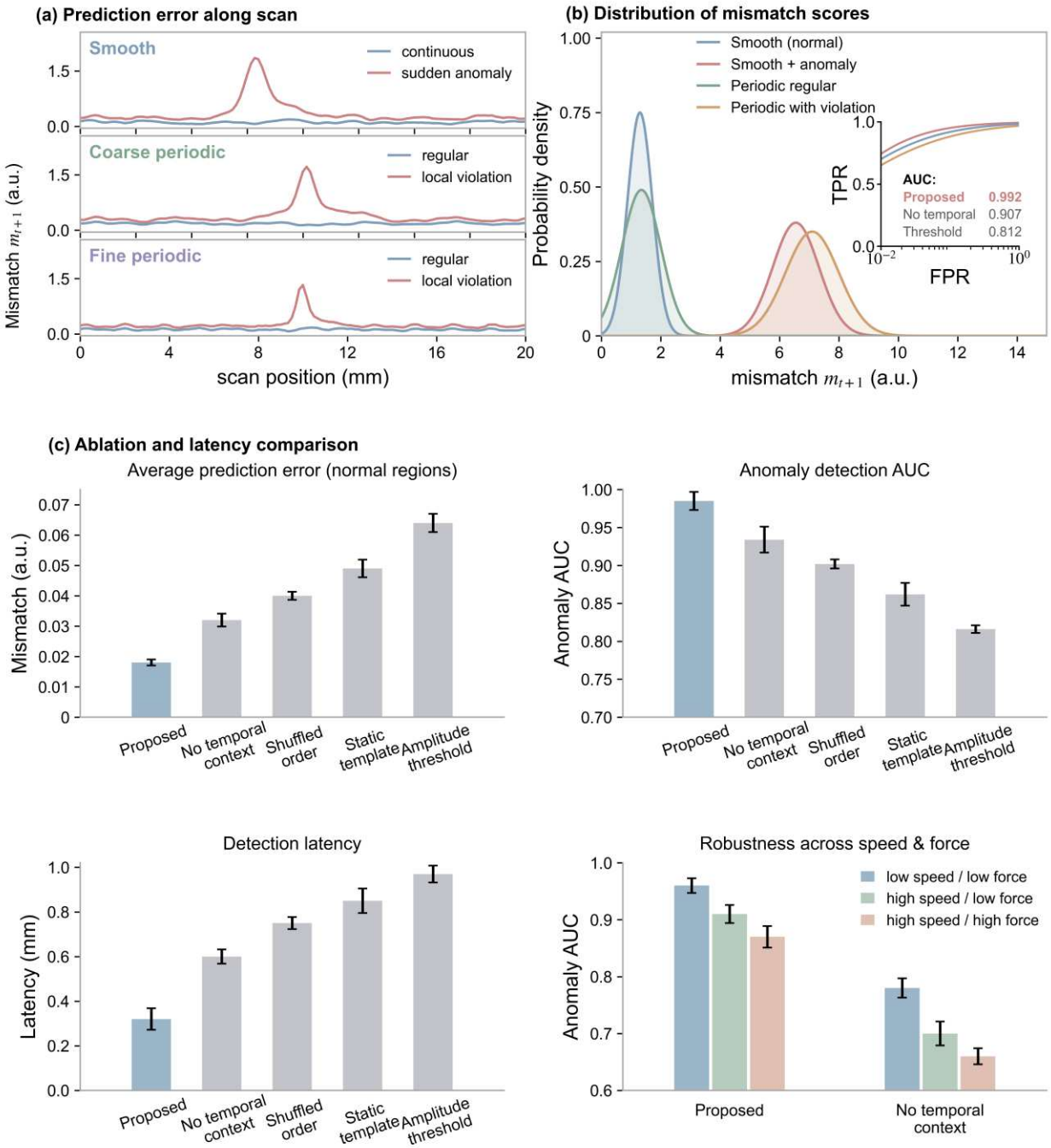


Figure 5 | Predictive mismatch trajectories, score distributions, and quantitative comparison. (a) Mismatch trajectories along scan position for smooth, coarse-periodic, and fine-periodic states, each comparing regular and violated conditions. **(b)** Distribution of mismatch scores for smooth and periodic states, together with pooled ROC comparison. **(c)** Quantitative comparison across baselines, including average prediction error in normal regions, anomaly-detection AUC, distance-to-detection, and robustness under three speed/force perturbation conditions.